figures. Consistent results were obtained by these two techniques. From the pole figures of normals to the (120) and (032) planes of PEO (27), it is seen that there is no preferred orientation of crystals in the control film except for a slight orientation due to the extrusion process (Fig. 3A). In Fig. 3B, the film with 3.6-μm-thick PEO layers also showed only very weak orientation. In contrast, the film with 110-nm-thick PEO layers showed a very strong orientation of the (120) and also the (032) planes (Fig. 3C). Nearly all the (120) planes that contained polymer chains were perpendicular to the film plane. This meant that the fold surfaces of the lamellar PEO crystals were in the plane of the layer. Upon decreasing the PEO layer thickness to 20 nm, the preferred orientation of PEO lamellae parallel to the layers seemed even stronger, as indicated by the narrower ring at the pole figure circumference (Fig. 3D). The (120) planes were distributed evenly in the plane of film, always being perpendicular to the film surface. The pole figures for (032) normal in Fig. 3, C and D, resembled rings exactly offset by 67°, as predicted by the crystallographic unit cell for the preferred orientation of PEO lamellae parallel to the layer interface (16). Again, the ring for the (032) normal in Fig. 3D was much narrower than in Fig. 3C.

The crystal orientation of PEO in confined nanolayers essentially reproduced the crystal structure of PEO blocks in self-assembled PS-*b*-PEO diblock copolymers (14, 16). Comparing the sharpness of the WAXS pattern, considerably higher orientation was achieved by physically confining a high-molecular-weight PEO between force-assembled layers than by confining a low-molecular-weight PEO block between self-assembled lamellae with covalent links. When the thickness confinement occurred on the size scale of the usual lamellar thickness, the PEO layers crystallized as single lamellae with extremely large aspect ratios. It was suggested that the lamellae could be thought of as large, impermeable single crystals.

The coextrusion process, which operates with readily available polymers, now makes it possible to fabricate nanolayered polymeric structures in sufficient quantities to probe the structure-property relationships of the morphologies resulting from nanoscale confinement. For design and execution of packaging strategies, polymer nanolayers can be incorporated into conventional polymeric films with the right barrier properties for less cost, which in turn may reduce the environmental and energy impact.

### References and Notes

1. D. C. Bassett, *Principles of Polymer Morphology* (Cambridge Univ. Press, Cambridge, 1981).
2. D. H. Weinkauf, D. R. Paul, in *Barrier Polymers and Structures*, W. J. Koros, Ed. (American Chemical Society, Washington, DC 1990), pp. 60–91.
3. A. Hiltner, R. Y. F. Liu, Y. S. Hu, E. Baer, *J. Polym. Sci. Pt. B Polym. Phys.* **43**, 1047 (2005).
4. C. W. Frank et al., *Science* **273**, 912 (1996).
5. S. Goffri et al., *Nat. Mater.* **5**, 950 (2006).
6. G. Reiter et al., *Lect. Notes Phys.* **714**, 179 (2007).
7. E. Baer, A. Hiltner, H. D. Keith, *Science* **235**, 1015 (1987).
8. I. W. Hamley et al., *Macromolecules* **29**, 8835 (1996).
9. T. E. Bernal-Lara, R. Y. F. Liu, A. Hiltner, E. Baer, *Polymer (Guildf.)* **46**, 3043 (2005).
10. Y. Jin et al., *J. Polym. Sci. Pt. B Polym. Phys.* **42**, 3380 (2004).
11. R. M. Ho et al., *Macromolecules* **37**, 5985 (2004).
12. Y. S. Sun et al., *Macromolecules* **39**, 5782 (2006).
13. U. Mukai, R. E. Cohen, A. Bellare, R. J. Albalak, *J. Appl. Polym. Sci.* **70**, 1985 (1998).
14. M.-S. Hsiao et al., *Macromolecules* **41**, 8114 (2008).
15. Y. Ma, W. Hu, G. Reiter, *Macromolecules* **39**, 5159 (2006).
16. L. Zhu et al., *J. Am. Chem. Soc.* **122**, 5957 (2000).
17. S. Napolitano, M. Wübbenhorst, *J. Phys. Condens. Matter* **19**, 205121 (2007).
18. B. Li, A. R. Esker, *Langmuir* **23**, 2546 (2007).
19. F. S. Bates, G. H. Fredrickson, *Annu. Rev. Phys. Chem.* **41**, 525 (1990).
20. Z.-R. Chen, J. A. Kornfield, S. D. Smith, J. T. Grothaus, M. M. Satkowski, *Science* **277**, 1248 (1997).
21. G. M. Whitesides, B. Grzybowski, *Science* **295**, 2418 (2002).
22. R. Y. F. Liu, Y. Jin, A. Hiltner, E. Baer, *Macromol. Rapid Commun.* **24**, 943 (2003).
23. R. Y. F. Liu, T. E. Bernal-Lara, A. Hiltner, E. Baer, *Macromolecules* **37**, 6972 (2004).
24. 1 Barrer = $10^{10} \frac{cm^3 (STP) cm}{cm^2 \, s \, cmHg}$, where STP is standard temperature and pressure.
25. P. H. Geil, *Polymer Single Crystals* (Wiley-Interscience, New York, 1963).
26. E. L. Cussler, S. E. Hughes, W. J. Ward III, R. Aris, *J. Membr. Sci.* **38**, 161 (1988).
27. The PEO reflection labeled (032) actually contains overlapped reflections from (032), ($\bar{1}$32), (112), ($\bar{2}$12), ($\bar{1}$24), ($\bar{2}$04), and (004), which have similar *d*-spacing of ~0.39 nm, with that from (032) being the strongest. They cannot be easily separated in (032) pole figure. Details can be found in (16).
28. This research was supported by the NSF Center for Layered Polymeric Systems (grant DMR-0423914).

# Nitrogen-Doped Carbon Nanotube Arrays with High Electrocatalytic Activity for Oxygen Reduction

Kuanping Gong,[1] Feng Du,[1] Zhenhai Xia,[2] Michael Durstock,[3] Liming Dai[1,4]*

The large-scale practical application of fuel cells will be difficult to realize if the expensive platinum-based electrocatalysts for oxygen reduction reactions (ORRs) cannot be replaced by other efficient, low-cost, and stable electrodes. Here, we report that vertically aligned nitrogen-containing carbon nanotubes (VA-NCNTs) can act as a metal-free electrode with a much better electrocatalytic activity, long-term operation stability, and tolerance to crossover effect than platinum for oxygen reduction in alkaline fuel cells. In air-saturated 0.1 molar potassium hydroxide, we observed a steady-state output potential of −80 millivolts and a current density of 4.1 milliamps per square centimeter at −0.22 volts, compared with −85 millivolts and 1.1 milliamps per square centimeter at −0.20 volts for a platinum-carbon electrode. The incorporation of electron-accepting nitrogen atoms in the conjugated nanotube carbon plane appears to impart a relatively high positive charge density on adjacent carbon atoms. This effect, coupled with aligning the NCNTs, provides a four-electron pathway for the ORR on VA-NCNTs with a superb performance.

The oxygen reduction reaction (ORR) at the cathode of fuel cells (1) plays a key role in controlling the performance of a fuel cell, and efficient ORR electrocatalysts are essential for practical applications of the fuel cells (2, 3). The ORR can proceed either through (i) a four-electron process to combine oxygen with electrons and protons directly, when coupled with oxidation on the anode, to produce water as the end product, or (ii) a less efficient two-step, two-electron pathway involving the formation of hydrogen peroxide ions as an intermediate (2, 3). Alkaline fuel cells with platinum-loaded carbon as an electrocatalyst for the four-electron ORR were developed for the Apollo lunar mission in the 1960s (4), but their large-scale commercial application has been precluded by the high cost of the requisite noble metals. Apart from its high cost, the Pt-based electrode also suffers from its susceptibility to time-dependent drift (5) and CO deactivation (6).

Recent intensive research efforts in reducing or replacing Pt-based electrode in fuel cells have led to the development of new ORR electrocatalysts, including Pt-based alloys (7), transition metal chalcogenides (8), carbon nanotube–supported metal particles (9–11), enzymatic electrocatalytic systems (12), and even conducting poly(3,4-

[1]Departments of Chemical and Materials Engineering, University of Dayton, 300 College Park, Dayton, OH 45469, USA. [2]Department of Mechanical Engineering, University of Akron, Akron, OH 44325, USA. [3]Materials and Manufacturing Directorate, Air Force Research Laboratory, RXBP, Wright-Patterson Air Force Base, OH 45433, USA. [4]Department of Chemistry and University of Dayton Research Institute and Institute for the Development and Commercialization of Advanced Sensor Technology and Wright Brothers Institute, Dayton, OH 45469, USA.

*To whom correspondence should be addressed. E-mail: ldai@udayton.edu

ethylenedioxythiophene) (PEDOT)–coated membranes (*13*). Apart from their use as the noble metal–catalyst supports (*9–11*), aligned carbon nanotubes formed by high-temperature treatment of certain metal heterocyclic molecules (e.g., ferrocene/NH₃) have been recently demonstrated to show some ORR electrocatalytic activities (*10*). The observed electrocatalytic activity was attributed to the presence of FeN₂-C and/or FeN₄-C active sites in the nanotube structure (*10*). However, we found in this study that vertically aligned nitrogen-containing carbon nanotubes (VA-NCNTs) produced by pyrolysis of iron(II) phthalocyanine (a metal heterocyclic molecule containing nitrogen) (*14*), in either the presence or absence of additional NH₃ vapor (*15*), could be used as effective ORR electrocatalysts, even after a complete removal of the residual Fe catalyst by electrochemical purification [supporting online material (SOM) (*16*)]. These metal-free VA-NCNTs were shown to catalyze a four-electron ORR process with a much higher electrocatalytic activity, lower overpotential (the difference between thermodynamic and formal potentials), smaller crossover effect, and better long-term operation stability than that of commercially available or similar platinum-based electrodes (C2-20, 20% platinum on Vulcan XC-72R; E-TEK) in alkaline electrolytes (*17, 18*).

A cross-sectional scanning electron microscopy (SEM) view for the as-synthesized VA-NCNT array is shown in Fig. 1A. The observed zigzag-like path along the nanotube length can be attributed to the integration of nitrogen into the graphitic structure to alter the nanotube surface from a straight cylinder geometry (*10*). The presence of structural nitrogen was confirmed by x-ray photoelectron spectroscopic (XPS) measurements (fig. S2) (*16*), which show the incorporation of pyridinic-like (399 eV) and pyrrolic-like (401 eV) nitrogen atoms within the nanotube graphene sheets with a N:C atomic ratio in the range of ~4 to 6 atomic % (table S1) (*16*). The aligned structure remained largely unchanged after the electrochemical purification (*16, 19*).

The corresponding transmission electron microscopy (TEM) image shows that, after electrochemical purification, the individual NCNTs are free from residual iron catalyst particles (Fig. 1B) (*16*). These NCNTs are about 8 μm long and 25 nm in outer diameter and exhibit a bamboo-like structure such as that seen for other CNTs (*14*). Figure 1C shows a digital photograph of the electrochemically purified VA-NCNT film after having
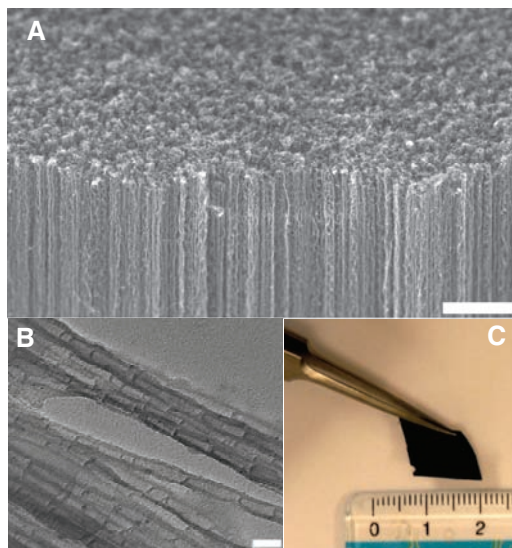


**Fig. 1. (A)** SEM image of the as-synthesized VA-NCNTs on a quartz substrate. **(B)** TEM image of the electrochemically purified VA-NCNTs. **(C)** Digital photograph of the VA-NCNT array after having been transferred onto a PS-nonaligned CNT conductive nanocomposite film (fig. Sl) (*16*). Scale bars, 2 μm (A); 50 nm (B).

**Fig. 2. (A)** CVs for oxygen reduction at the unpurified (upper) and electrochemically purified (bottom) VA-NCNT/GC electrodes in the argon-protected (dotted curves) or air-saturated 0.1 M KOH (solid red curves) at the scan rate of 100 mVs⁻¹. Before the measurements, the unpurified VA-NCNT/GC electrode was repeatedly potentiodynamic swept from +0.2 V to −1.2 V in an Ar-protected 0.1 M KOH until a steady voltammogram curve was obtained. **(B)** RRDE voltammograms and the corresponding amperometric responses for oxygen reduction in air-saturated 0.1 M KOH at the NA-CCNT/GC (curves 1 and 1′), Pt-C/GC (curves 2 and 2′), and NA-NCNT/GC (curves 3 and 3′) electrodes at the scan rate of 10 mVs⁻¹. The electrode rotation rate was 1400 revolutions per minute (rpm), and the Pt ring electrode was poised at 0.5 V. **(C)** RRDE voltammograms for oxygen reduction in air-saturated 0.1 M KOH at the Pt-C/GC (curve 1), VA-CCNT/GC (curve 2), and VA-NCNT (curve 3) electrodes. Because of the technical difficulties associated with the sample mounting, amperometic responses with the Pt ring electrode were not measured for the vertically aligned carbon nanotubes. **(D)** Calculated charge density distribution for the NCNTs. **(E)** Schematic representations of possible adsorption modes of an oxygen molecule at the CCNTs (top) and NCNTs (bottom). The C atoms around the pyrrolic-like nitrogen could possess much higher positive charges than do the C atoms around the pyridinic-like nitrogen (fig. S6) (*16*).
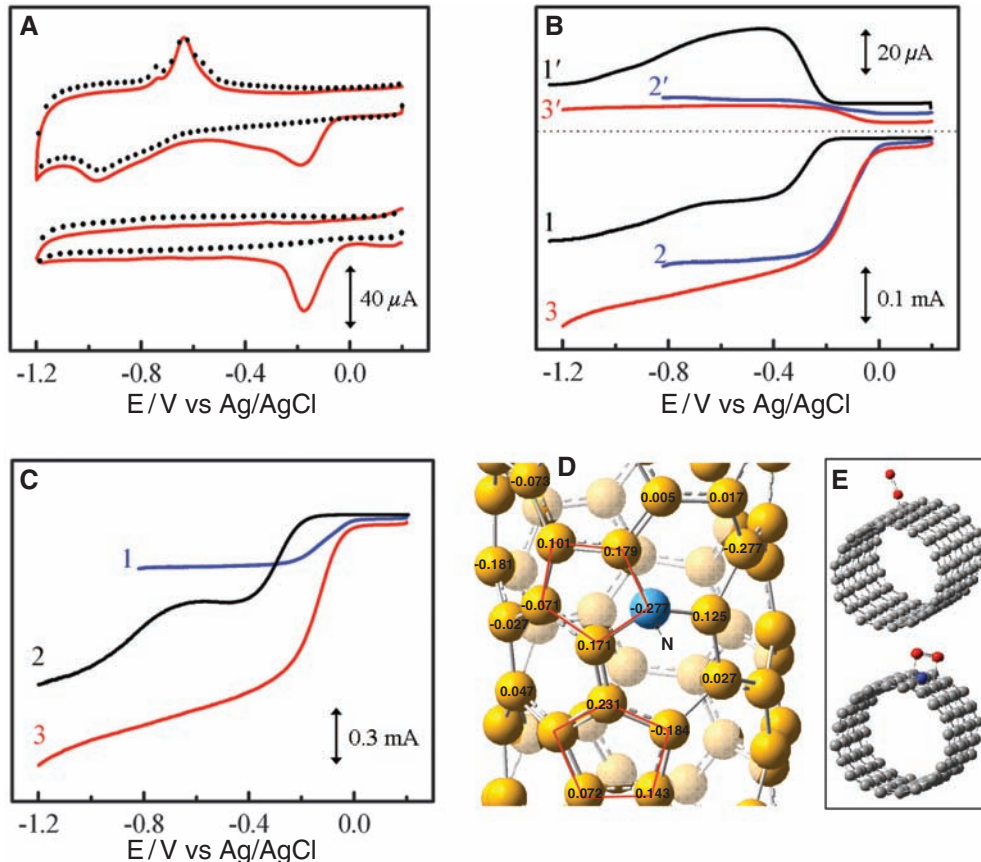
been transferred onto a polystyrene (PS)–nonaligned carbon nanotube conductive composite film to be used to cover the active area of a glassy carbon electrode for ORR (fig. S1) (16). The size of the free-standing VA-NCNT film thus prepared is limited mainly by the size of the furnace used for the aligned nanotube growth.

The electrochemical purification was confirmed by voltammetric responses of the VA-NCNT electrode before and after electrochemical oxidation (16). As shown in Fig. 2A, the cyclic voltammogram (CV) of the glassy carbon–supported aligned unpurified VA-NCNT electrode (VA-NCNT/GC) (fig. S1) (16) in an aqueous solution of 0.1 M KOH under argon protection (top dot curve in Fig. 2A) exhibited two well-defined peaks at the potential of about –1.0 V and –0.65 V, arising from redox reactions associated with the Fe catalyst residues (20). In contrast, the corresponding voltammetric response for the same VA-NCNT/GC electrode after the electrochemical purification showed a featureless curve (bottom dot curve in Fig. 2A). This difference strongly suggests that the iron catalyst residues have been largely removed by the electrochemical oxidation, as also evidenced by XPS (fig. S2) (16) and thermogravimetric analyses (fig. S3) (16).

Also shown in Fig. 2A are CVs for oxygen reduction in 0.1 M KOH solution at the VA-NCNT/GC before (top solid red curve) and after (bottom solid red curve) the electrochemical purification. Unlike conventional carbon electrodes (21), a cathodic process with a rather high reduction potential (i.e., lower overpotential) of about –0.15 V was seen for the ORR at both the unpurified and electrochemically purified VA-NCNT/GC electrodes with some notable difference in the peak shape. To gain further insight on the ORR electrochemical procedures, we performed rotating ring-disk electrode (RRDE) voltammograms. Figure 2B shows the steady-state voltammograms for nitrogen-free nonaligned carbon nanotubes supported by a glassy carbon electrode (NA-CCNT/GC, curve 1), commercially available platinum-loaded carbon (Vulcan XC-72R) supported by a glassy carbon electrode (Pt-C/GC, curve 2), and glassy carbon–supported nonaligned nitrogen-containing carbon nanotubes (NA-NCNT/GC, curve 3) in air-saturated 0.1 M KOH electrolyte. The corresponding amperometric responses (curves 1′ to 3′) for the oxidation of hydrogen peroxide ions (HO$_2^-$) measured with a Pt ring electrode at the potential of 0.50 V (16) are also included in Fig. 2B. The NA-CCNT/GC electrode showed a two-step process for ORR with the onset potential of about –0.22 V and –0.70 V, respectively (curve 1 in Fig. 2B), consistent with previous reports (8, 21). We attribute the first sharp step over –0.22 V to the two-electron reduction of O$_2$ to HO$_2^-$, as evidenced by a substantial concomitant increase in the oxidation current over about –0.22 to –0.41V at the ring electrode (curve 1′ in Fig. 2B). The subsequent gradual decrease in

the ring current seen in curve 1′ of Fig. 2B corresponds to the reduced amount of HO$_2^-$ reached to the ring electrode before being oxidized into HO$^-$ at the disk electrode under the increased negative potentials.

Unlike the NA-CCNT/GC electrode, the NA-NCNT/GC electrode exhibited a one-step process for the ORR with the steady-state diffusion current that was almost twice that obtained at the NA-CCNT/GC electrode (curves 1 and 3 in Fig. 2B). Like the Pt-C/GC electrode, the observed one-step process suggests a four-electron pathway for the ORR at the NA-NCNT/GC electrode, as also supported by the corresponding negligible current for HO$_2^-$ oxidation recorded at the Pt ring electrode (curve 3′ in Fig. 2B). The transferred electron number (n) per oxygen molecule involved in the ORR was calculated from Eq. 1 (22) to be 1.8 and 3.9 for the NA-CCNT/GC electrode (at the potential of –0.40 V) and the NA-NCNT/GC electrode (at the potential of –0.30 V), respectively.

$$n = 4I_D/(I_D + I_R/N) \qquad (1)$$

where N = 0.3 is the collection efficiency (16), I$_D$ is the faradic disk current, and I$_R$ is the faradic ring current.

Figure 2C shows the steady-state voltammograms for Pt-C/GC (curve 1), VA-CCNT/GC (curve 2), and VA-NCNT/GC (curve 3) electrodes in the air-saturated 0.1 M KOH electrolyte.

The half-wave potentials for ORR at the NA-NCNT/GC (curve 3, Fig. 2B) and VA-NCNT/GC electrodes (curve 3 in Fig. 2C) are comparable to that at the Pt-C/GC electrode (–0.1 V), but a substantially enhanced steady-state diffusion current (~0.8 mA) was observed over a large potential range for the VA-NCNT/GC electrodes with respect to the Pt-C/GC electrode (Fig. 2C). Thus, the VA-NCNT/GC electrode is much better than the Pt-C/GC electrode for the ORR in an alkaline solution. Compared with the NA-NCNT/GC electrode, the better electrocatalytic performance of the VA-NCNT/GC electrode can be attributed to its well-defined large surface area with all of the nanotube top-ends falling on one plane at the interface between the aligned nanotube electrode and electrolyte solution to further facilitate the electrolyte/reactant diffusion (23, 24). Similar current enhancement by the alignment structure was also observed for the VA-CCNT/GC electrode (curve 2 in Fig. 2C) with respect to its nonaligned counterpart (curve 1 in Fig. 2B), albeit with a relatively small effect and at a very high overpotential. The similar shape of the steady-state voltammograms for the aligned nanotube electrodes and their respective nonaligned counterparts indicates that the electrochemical mechanism for the ORR is insensitive to the alignment structure, although alignment can improve the electrokinetics. However, the much stronger diffusion-limited currents and lower overpotentials observed for the NCNT electrodes than their nitrogen-free counterparts indicate the importance of the nitrogen het-
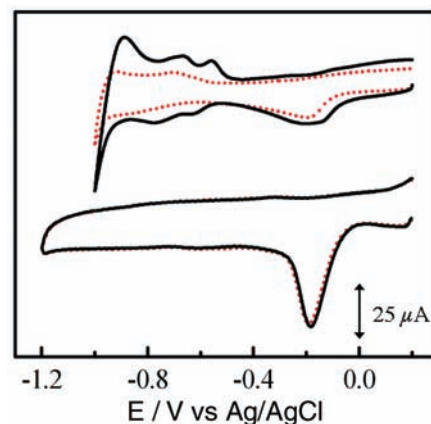


**Fig. 3.** CVs for the ORR at the Pt-C/GC (top) and VA-NCNT/GC (bottom) electrodes before (solid black curves) and after (dotted curves) a continuous potentiodynamic swept for ~100,000 cycles in an air-saturated 0.1 M KOH at room temperature (25 ± 1°C). Scan rate, 100 mV s$^{-1}$. The wavelike bands over −1.0 to −0.5 V seen for the pristine Pt-C/GC electrode are attributable to hydrogen adsorption/desorption.

eroatoms in the NCNTs (fig. S2) (16) to their electrocatalytic activities for the ORR.

Quantum mechanics calculations with B3LYP hybrid density functional theory (Gaussian 03) (25) indicate that carbon atoms adjacent to nitrogen dopants possess a substantially high positive charge density to counterbalance the strong electronic affinity of the nitrogen atom (Fig. 2D and figs. S5 and S6) (16). Together with the recent work on the metal-free conjugated PEDOT ORR electrode (13), this result prompted us to put forward an O$_2$ reduction mechanism on the NCNT electrodes. A redox cycling process reduces the carbon atoms that naturally exist in an oxidized form by the action of the electrochemical cycling, followed by reoxidation of the reduced carbon atoms to their preferred oxidized state upon O$_2$ absorption. The nitrogen-induced charge delocalization could also change the chemisorption mode of O$_2$ from the usual end-on adsorption (Pauling model) at the CCNT surface (top, Fig. 2E) to a side-on adsorption (Yeager model) onto the NCNT electrodes (bottom, Fig. 2E) (26). The parallel diatomic adsorption could effectively weaken the O–O bonding to facilitate ORR at the NCNT/GC electrodes. As such, doping carbon nanotubes with nitrogen heteroatoms as in the NCNT electrodes can efficiently create the metal-free active sites for electrochemical reduction of O$_2$.

To investigate the stability of the VA-NCNT/GC electrode toward ORR, we performed continuous potential cycling between +0.2 and –1.2 V for the VA-NCNT/GC electrode with Pt-C/GC as reference in air-saturated 0.1 M KOH for ~100,000 cycles. As can be seen in Fig. 3, the deterioration of Pt occurred, apart from the ORR, on the commercial Pt-C/GC (Vulcan XC-72) electrode (top curves) (27). The continuous po-
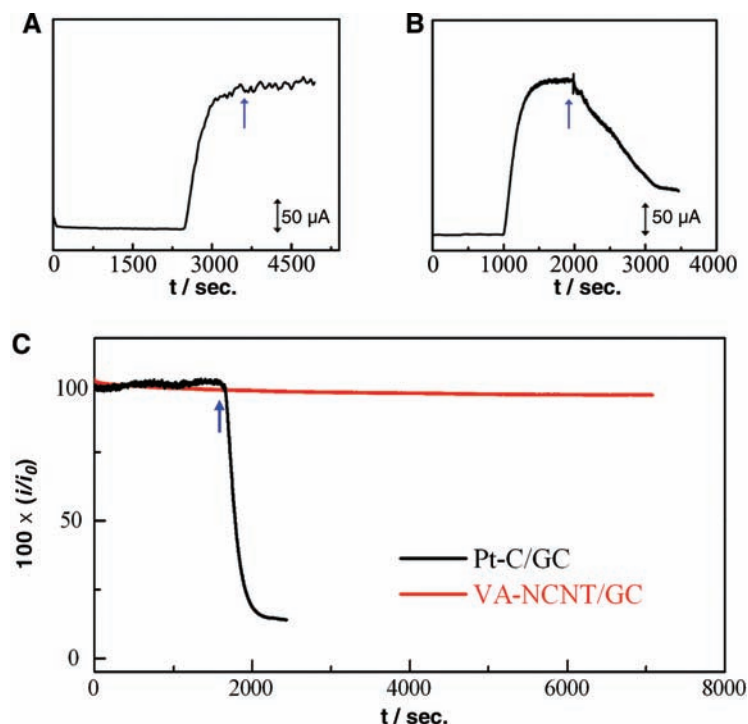
**Fig. 4. (A)** *i-t* chronoamperometric responses obtained at the VA-NCNT/GC electrode at −0.25 V in 0.1 M KOH under magnetic stirring (1000 rpm, MR 3001 K, Heidolph) and Ar-protection over 0 to 2400 s, followed by an immediate introduction of air. The arrow indicates the sequential addition of 3.0 M glucose, 3.0 M methanol, and 3.0 M formaldehyde, respectively, into the air-saturated electrochemical cell (fig. S1B) (*16*). **(B)** Corresponding *i-t* chronoamperometric response obtained at the Pt-C/GC electrode with the addition of 3.0 M methanol (as indicated by the arrow) after exposure to air at 1000 s under the same conditions as in (A) for comparison. **(C)** CO-poison effect on the *i-t* chronoamperometric response for the Pt-C/GC and VA-NCNT/GC electrodes. The arrow indicates the addition of 55 mL/min CO gas into the 550 mL/min $O_2$ flow; the mixture gas of ~9% CO (volume/volume) was then introduced into the electrochemical cell (fig. S1B) (*16*). $i_0$, initial current.

for the relatively low-cost production of carbon nanotubes continues to grow, the price of carbon nanotubes is expected to further decrease (*33*). The role of nitrogen-doping demonstrated in this study could be applied to the design and development of various other metal-free efficient ORR catalysts, and these nitrogen-containing carbon nanotube electrodes are clearly of practical importance.

**References and Notes**
1. B. C. H. Steele, A. Heinzel, *Nature* **414**, 345 (2001).
2. S. Basu, Ed., *Recent Trends in Fuel Cell Science and Technology* (Springer, New York, 2007).
3. B. Sljukic, C. E. Banks, R. G. Compton, *J. Iranian Chem. Soc.* **2**, 1 (2005).
4. http://americanhistory.si.edu/fuelcells/alk/alk3.htm (copyright 2001, Smithsonian Institution).
5. X. Yu, S. Ye, *J. Power Sources* **172**, 145 (2007).
6. M. Winter, R. J. Brodd, *Chem. Rev.* **104**, 4245 (2004).
7. J. Zhang, K. Sasaki, E. Sutter, R. R. Adzic, *Science* **315**, 220 (2007).
8. K. Gong, P. Yu, L. Su, S. Xiong, L. Mao, *J. Phys. Chem. C* **111**, 1882 (2007).
9. G. Che, B. B. Lakshmi, E. R. Fisher, C. R. Martin, *Nature* **393**, 346 (1998).
10. J. Yang, D.-J. Liu, N. N. Kariuki, L. X. Chen, *Chem. Commun. (Cambridge)* 329 (2008).
11. A. Kongkanand, S. Kuwabata, G. Girishkumar, P. Kamat, *Langmuir* **22**, 2392 (2006).
12. J. P. Collman *et al.*, *Science* **315**, 1565 (2007).
13. B. Winther-Jensen, O. Winther-Jensen, M. Forsyth, D. R. MacFarlane, *Science* **321**, 671 (2008).
14. L. Dai *et al.*, *ChemPhysChem* **4**, 1150 (2003), and references therein.
15. L. S. Panchakarla, A. Govindaraj, C. N. R. Rao, *ACS Nano* **1**, 494 (2007).
16. Supporting materials are available on *Science* Online.
17. Z. Chen, M. Waje, W. Li, Y. Yan, *Angew. Chem. Int. Ed.* **46**, 4060 (2007).
18. S. H. Joo *et al.*, *Nature* **412**, 169 (2001).
19. M. Gao *et al.*, *Angew. Chem. Int. Ed.* **39**, 3664 (2000).
20. U. Casellato, N. Comisso, G. Mengoli, *Electrochim. Acta* **51**, 5669 (2006).
21. M. Zhang *et al.*, *Langmuir* **20**, 8781 (2004).
22. S. L. Gupta, D. Tryk, W. Aldred, E. Yeager, in *Proceedings of the Symposium on Load Levelling and Energy Conservation in Industrial Processes*, D. Chin, Ed. (Electrochemical Society, Pennington, NJ, 1986), p. 207.
23. L. Dai, Ed., *Carbon Nanotechnology: Recent Developments in Chemistry, Physics, Materials Science and Device Applications* (Elsevier, Amsterdam, 2006).
24. L. Dai, *Aust. J. Chem.* **60**, 472 (2007), and references therein.
25. M. J. Fisch *et al.*, *Gaussian 03*, Revision B.04 (Gaussian, Pittsburgh, PA, 2003).
26. Z. Shi, J. Zhang, Z. Liu, H. Wang, D. P. Wilkinson, *Electrochim. Acta* **51**, 1905 (2006).
27. E. H. Yu, K. Scott, R. W. Reeve, *Fuel Cells (Weinheim)* **3**, 169 (2003).
28. The methanol oxidation on the anode is a competitive reaction to oxygen reduction at the cathode in a direct methanol fuel cell. Because the oxidation of fuels on noble-metal electrodes often commences at a potential lower than that of the ORR under the working conditions, methanol crossover from the anode to the cathode, if not eliminated, could diminish the cathodic performance through the depolarizing effect. Furthermore, it may even cause the whole fuel-cell system to be paralyzed through poisoning the ORR electrocatalyst by CO-like species generated as intermediates of the methanol oxidation at the cathode (*29*).
29. A. S. Arico, S. Srinivasan, V. Antonucci, *Fuel Cells (Weinheim)* **1**, 133 (2001).
30. H.-F. Cui, J.-S. Ye, X. Liu, W.-D. Zhang, F.-S. Sheu, *Nanotechnology* **17**, 2334 (2006).
31. J. J. Gooding *et al.*, *Electrochem. Commun.* **9**, 1677 (2007).
32. V. H. Ebron *et al.*, *Science* **311**, 1580 (2006).

tential cycling might have caused migration/aggregation of the Pt nanoparticles and subsequent loss of the specific catalytic activity. In contrast, the VA-NCNT/GC electrode showed almost identical voltammetric responses before and after the continuous potential cycling under the same condition (bottom curves in Fig. 3).

The VA-NCNT/GC electrode was further subjected to testing the possible crossover and poison effects in the presence of fuel molecules (e.g., methanol) and CO, respectively (*27–29*). To examine the possible crossover effect, we measured electrocatalytic selectivity of the VA-NCNT/GC electrode against the electrooxidation of various commonly used fuel molecules, including hydrogen gas, glucose, methanol, and formaldehyde (Fig. 4A). For comparison, the corresponding current-time (*i-t*) chronoamperometric response for a Pt-C/GC electrode given in Fig. 4B shows a sharp decrease in current upon the addition of 3.0 M methanol. However, the strong and stable amperometric response from the ORR on the VA-NCNT/GC electrode remained unchanged after the sequential addition of hydrogen gas, glucose, methanol, and formaldehyde (Fig. 4A). Such high selectivity of the VA-NCNT/GC electrode toward the ORR and remarkably good tolerance to crossover effect for

the VA-NCNT/GC electrode can be attributed to the much lower ORR potential than that required for oxidation of the fuel molecules (*30*) and is further evidenced by the cathodic polarization measurements in the presence and absence of 3.0 M methanol (fig. S4) (*16*).

The effect of CO on the electrocatalytic activity of the VA-NCNT/GC electrode was also tested because CO poisoning of most noble-metal electrodes is a major issue in the current fuel cell technology. Being nonmetallic, the VA-NCNT/GC electrode was insensitive to CO poisoning even after adding about 10% CO in oxygen (red line in Fig. 4C), whereas the Pt-C/GC electrode was rapidly poisoned under the same conditions (black curve in Fig. 4C). This result indicates that the VA-NCNT/GC electrode is free from residual iron particles, as iron-based catalysts would otherwise be readily poisoned by CO (*6*).

The high–surface area, good electrical and mechanical properties, and superb thermal stability intrinsically characteristic of aligned carbon nanotubes (*23*, *31*, *32*) provide additional advantages for the nanotube electrode to be used in fuel cells under both ambient and harsh conditions. Although cost depends on many factors, scarcity is not an intrinsic issue for carbon nanotubes. As the number of industrial-scale facilities

33. The price for multiwall carbon nanotubes has dropped from a few hundred U.S. dollars per gram in the 1990s to about 100 U.S. dollars per kilogram. See, for example, http://www.azonano.com/details.asp?ArticleID=1108.
34. We gratefully acknowledge financial support for this work from the Air Force Office of Scientific Research (grant

# Anomalously Metal-Rich Fluids Form Hydrothermal Ore Deposits

Jamie J. Wilkinson,[1,2]*† Barry Stoffell,[1]‡ Clara C. Wilkinson,[1,2]†
Teresa E. Jeffries,[2] Martin S. Appold[3]

Hydrothermal ore deposits form when metals, often as sulfides, precipitate in abundance from aqueous solutions in Earth's crust. Much of our knowledge of the fluids involved comes from studies of fluid inclusions trapped in silicates or carbonates that are believed to represent aliquots of the same solutions that precipitated the ores. We used laser ablation inductively coupled plasma mass spectrometry to test this paradigm by analysis of fluid inclusions in sphalerite from two contrasting zinc-lead ore systems. Metal contents in these inclusions are up to two orders of magnitude greater than those in quartz-hosted inclusions and are much higher than previously thought, suggesting that ore formation is linked to influx of anomalously metal-rich fluids into systems dominated by barren fluids for much of their life.

Hydrothermal ore deposits, formed from the flow of hot solutions through porous or fractured rocks, are the principal source of metals in Earth's crust (*1*). Such large accumulations of metal require concentration of elements hundreds or thousands of times above natural abundance, implying high-mass fluxes through small volumes of rock coupled with efficient precipitation. A fundamental control on the formation of hydrothermal deposits is the ability of the fluid to carry metals in solution (*2*). Yet, paradoxically, for most deposit types formed at low-to-intermediate temperatures, both direct analysis of fluid inclusions and theoretical calculation indicate that the concentrations of dissolved metals are likely to be low, on the order of tens of parts per million (*3*). Also, samples of modern crustal fluids, such as those from oil fields or mid-ocean ridges, typically contain only a few parts per million of Cu, Zn, and Pb (*4*, *5*), although there are exceptions, such as the Salton Sea geothermal brines in California (*6*) and oil-field waters from central Mississippi (*4*). A consequence is that the other parameters that govern total metal flux in ore formation (average flow velocity and system lifetime) tend toward their

likely geological limits in both numerical simulations and empirical models based on geological and geochronological constraints (*7*, *8*). As a result, it has been suggested that higher-than-normal concentrations of metal in fluids may be required to form large ore bodies (*9*).

For several decades, a key source of information on the physical and chemical conditions of hydrothermal ore formation has been fluid inclusions trapped during mineral growth (*10*). In most deposits, metalliferous ore minerals (commonly opaque sulfides) occur together with uneconomic transparent phases (gangue). Because fluid inclusions in the opaque phases are not easily studied by traditional transmitted light microscopy and microanalytical methods, the nature of ore-forming fluids and the conditions of ore-mineral precipitation have often been inferred from the properties of inclusions trapped in the associated gangue minerals. However, it is often difficult to provide unequivocal evidence for coprecipitation based on textural observations or isotopic measurements (*11*); consequently, uncertainty remains concerning the temporal and, therefore, genetic relationship between gangue-hosted inclusions and the ore-forming process. Several studies that used infrared light microscopy to observe inclusions in opaque minerals such as wolframite and cassiterite have shown that the properties of these fluid inclusions may, indeed, be different (*12*).

We analyzed fluid inclusions in sphalerite (ZnS) from two zinc-lead ore systems with the use of laser ablation inductively coupled plasma mass spectrometry (LA-ICPMS). Primary inclusions in sphalerite must represent the ore-forming fluid because they are trapped during growth of the ore mineral itself. Unlike bulk analytical studies that are limited to a few major elements

and that may sample multiple populations of inclusions (*13*), LA-ICPMS allows determination of trace elements (including ore metals) in single, texturally constrained inclusions.

We selected samples from two well-studied hydrothermal ore systems. The Northern Arkansas district of the Ozark Plateau, North America, is an example of low-temperature Mississippi Valley–Type (MVT) zinc-lead mineralization, thought to have formed by continent-scale basinal brine migration (*14*). The Midlands Basin orefield in Ireland contains several large zinc-lead(-barium) ore deposits formed from moderate temperature fluids generated by deep crustal circulation of seawater-derived brines during continental rifting (*15*, *16*). Both systems are economically noteworthy but provide a contrast in terms of sources of metals, sulfur, and hydrological regime. Lead is of particular interest because it needs to be concentrated above average crustal abundance more than any other common ore-forming element (~4000 times) to form a potentially economic accumulation.

Samples from Northern Arkansas were collected from exposures in the Monte Cristo and Philadelphia Mines of the Rush subdistrict and from the Lucky Dog Mine of the Tomahawk Creek subdistrict. They comprise fine- to coarse-grained crystalline quartz and medium- to coarse-grained pale yellow–to–brown sphalerite. Regionally, precipitation of sphalerite typically overlapped with that of jasperoid and finely crystalline quartz, and more coarsely crystalline quartz formed later (*17*). Samples from Ireland were collected from historic mine exposures and drill core from the Silvermines deposit, as well as from quarry outcrop of quartz-sulfide veins nearby. The deposit samples are composed of massive sulfide dominated by coarse-grained brown sphalerite that replaces early disseminated granular and framboidal pyrite. The vein sample is composed of quartz and ankerite, as well as minor sphalerite and galena, and was selected as a representative example of a regionally developed set of feeder veins developed underneath the ore deposits (*18*, *19*).

Salinity data derived from freezing experiments (*20*) show that the Northern Arkansas mineralization formed from brines, typical of MVT deposits (Fig. 1). Assuming fluids were trapped at hydrostatic pressure at depths of <2 km, the inferred depth of ore formation (*14*), we calculated an isochoric correction of <+10°C to recorded homogenization temperature ($T_h$) values to give true trapping temperatures. Thus, $T_h$ can be regarded as a reasonable approximation of fluid temperature during mineral growth. Inclusions from the Irish samples display lower salin-

[1]Department of Earth Science and Engineering, Imperial College London, South Kensington Campus, Exhibition Road, London SW7 2AZ, UK. [2]Department of Mineralogy, Natural History Museum, Cromwell Road, London SW7 5BD, UK. [3]Department of Geological Sciences, University of Missouri–Columbia, 101 Geological Sciences Building, Columbia, MO 65211, USA.

*To whom correspondence should be addressed. E-mail: j.wilkinson@imperial.ac.uk
†Present address: Australian Research Council Centre of Excellence in Ore Deposits (CODES), Private Bag 126, University of Tasmania, Hobart, Tasmania 7001, Australia.
‡Present address: Rio Tinto Mining and Exploration Limited, 2 Eastbourne Terrace, London W2 6LG, UK.